Solar Energy Materials & Solar Cells 259 (2023) 112449

Contents lists available at ScienceDirect

Solar Energy Materials and Solar Cells

journal homepage: www.elsevier.com/locate/solmat

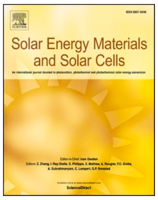

Tungsten nanodisc-based spectrally-selective polarization-independent thermal emitters

Anisha Chirumamilla [a,b,**], Fei Ding [c], Yuanqing Yang [c], Murugan Senthil Mani Rajan [d], Sergey I. Bozhevolnyi [c], Duncan S. Sutherland [a], Kjeld Pedersen [b], Manohar Chirumamilla [b,e,*]

[a] *Interdisciplinary Nanoscience Center (iNANO) and iMAT, Aarhus University, Aarhus, 8000, Denmark*
[b] *Department of Materials and Production, Aalborg University, Skjernvej 4A, Aalborg, 9220, Denmark*
[c] *Centre for Nano Optics, University of Southern Denmark, Campusvej 55, Odense, 5230, Denmark*
[d] *Department of Physics, Anna University, University College of Engineering, Ramanathapuram, 623513, India*
[e] *Institute of Optical and Electronic Materials, Hamburg University of Technology, Eissendorfer Strasse 38, Hamburg, 21073, Germany*

ARTICLE INFO

Keywords:
Thermal emitters
Spectral selectivity
Tungsten
Nanodiscs
Large-area nanofabrication
Thermophotovoltaics

ABSTRACT

Thermophotovoltaic (TPV) cells convert thermally emitted photons into electrical power using photovoltaic (PV) detectors. To realize highly efficient thermal energy harvesting using TPV conversion, high-temperature stable spectrally-selective emitters are needed. The deployment of TPV technology lags behind conventional solar-PV technology due to the lack of large-scale fabrication of efficient thermal emitters, which would preferentially emit in the PV cell absorption band. In this work, we demonstrate a simple large-area nanofabrication method based on the hole-mask colloidal lithography and sputtering, which allows one to fabricate tungsten (W) nanodisc spectrally-selective emitters (consisting of a metal-insulator-metal configuration) with a high emissivity below the InGaAsSb PV-cell cut-off wavelength of 2.25 μm and a gradually decreasing emissivity (down to $<$ 10%) in the mid-infrared region. Frequency-domain time-domain (FDTD) simulations reveal that the spectral selectivity is achieved due to the localized surface plasmon resonance of W nanodiscs strongly influenced by the insulator thickness. Importantly, the W emitters show thermal stability at temperatures of up to 1100 °C, and emissivity invariance to changes in polarization and incidence angles up to 65°. This work represents a significant step towards the realization of high-temperature stable efficient thermal emitters by a facile and cost-effective fabrication method, thereby promoting the implementation of photonic/plasmonic thermal emitters in the next-generation thermal energy harvesting systems. The method proposed in this study holds potential for scalability; however, empirical evidence to demonstrate this scalability has not yet been established. Subsequent studies are needed to confirm the scalability of the proposed method and its extensive applicability.

1. Introduction

Thermophotovoltaics (TPVs) [1–12] play a crucial role in converting heat into electrical energy by transforming thermal photons at infrared wavelengths into electrical current via the photovoltaic (PV) effect using low-bandgap PV cells, such as InGaAsSb, GaAs, etc [13]. Thermal radiation from a blackbody radiator spreads over a broad spectral range, most of which lies in the long-wavelength region for radiator temperatures below the eventual melting of constituent materials. These long-wavelength (low-energy or out-of-band) infrared photons cannot be converted into electrical currents if their wavelengths exceed the cut-off wavelength (typically >2.5 μm) of the PV cell. Instead, they are wasted, being absorbed by the PV cell module, and thus increase the PV cell temperature causing in turn a decrease in the open-circuit voltage of the PV cell, thereby its efficiency. In principle, low-energy photons can be recycled using spectral control elements such as a mirror behind the PV cell or a front surface filter [14–16]. A highly-reflective mirror coating at the back of the PV cell returns the low-energy photons to the emitter to reheat it. In contrast, the front surface filters are placed between the emitter and PV cell to immediately reflect the low-energy photons back to the emitter [17,18]. Although the spectral control elements provide a considerable improvement in the utilization of

---

* Corresponding author. Department of Materials and Production, Aalborg University, Skjernvej 4A, Aalborg, 9220, Denmark.

** Corresponding author. Department of Materials and Production, Aalborg University, Skjernvej 4A, Aalborg, 9220, Denmark.

E-mail addresses: anishac@mp.aau.dk (A. Chirumamilla), mch@mp.aau.dk (M. Chirumamilla).

https://doi.org/10.1016/j.solmat.2023.112449
Received 19 December 2022; Received in revised form 23 June 2023; Accepted 26 June 2023
Available online 1 July 2023

out-of-band photons of a non-selective emitters, the filters and mirrors still have a residual absorptivity resulting in a TPV system efficiency reduction compared to the selective emitters that are operating without any spectral control elements. Therefore, to avoid sub-bandgap photon energy losses, an ideal, spectrally-selective emitter should emit with the unitary emissivity ($\varepsilon = 1$) for $E > E_g$ and zero emissivity ($\varepsilon = 0$) for $E < E_g$, where E and E_g are the thermal photon energy and the bandgap energy of PV cell, respectively.

In thermal energy harvesting using TPV conversion, various thermal sources, such as waste heat scavenging from industries and chemical/nuclear processes, thermal energy storage, and distributed generation, are used to heat spectral selective emitters. According to the Stefan-Boltzmann law [19], the radiative power of a blackbody is proportional to T^4, while the Wien's displacement law states that the blackbody radiation reaches its maximum at a wavelength that is inversely proportional to the temperature. Therefore, heating the emitter at higher temperatures provides a considerably larger radiative power and, at the same time, allows to use of highly efficient wide bandgap PV cells. Spectrally-selective emitters based on plasmonic/photonic structures have been widely investigated to suppress the out-of-band photons [5,17,20–26]. Most of these structures were made by lithography patterning (electron/ion-beam) or fabrication procedures containing several processing steps. These fabrication methods are technically challenging, time-consuming, and thus expensive, and so far, they are not perceived to apply to large-scale deployment. Moreover, the resulting nanostructured configurations were typically impractical to fabricate over extensive areas, such as at the wafer-scale level, and hardly suitable for operation at elevated temperatures. Therefore, scalable and cost-effective facile nanofabrication methods amenable to producing temperature-resistant and spectrally-selective emitters are highly sought after in order to boost the TPV technology implementation.

Here, we demonstrate large-area fabrication of W nanodisc spectrally-selective emitters fabricated by a scalable and cost-effective hole-mask colloidal lithography (HCL) and sputtering techniques [27–29]. Refractory metal W is chosen owing to its high melting temperature of ~3400 °C [5,20,30,31]. The emitter design contains a metal-insulator-metal (MIM) structure of W (film)-Al_2O_3 (film)-W (disc) layers on a sapphire substrate, so that all constituent materials are refractory. The spectral selectivity of the emitter structure can be tuned over a broad spectral window by tailoring the film thickness of the Al_2O_3 insulator (spacer). The experimentally measured spectral response of the emitter is compared with theoretical calculations, identifying the resonance contributions of the W nanodisc and Al_2O_3 film thicknesses. The emitter is found to exhibit thermal stability up to the annealing temperatures of 1100 °C for 24 h duration in an Ar atmosphere under ambient pressure.

2. Materials and methods

2.1. Tungsten nanodisc emitter fabrication

As an initial step, a thick W layer of 150 nm was deposited onto a Sapphire (0001) substrate of 1.8×1.8 cm^2 size by DC sputtering at a rate of 0.3 Å/s. Afterwards, thin films of Al_2O_3 at various thicknesses (50–150 nm) were deposited using e-beam deposition at a rate of 0.3 Å/s. Later, 200 nm thick polymethyl methacrylate (PMMA) resist was spin-coated onto the W coated Sapphire substrate, and then patterns of short-range-ordered nanoholes were fabricated by hole-mask colloidal lithography. Hole-mask colloidal lithography provides short-range-ordered circular nanodiscs. The average spacing between the nanodiscs, along with their diameter and size distributions, were defined by the polystyrene nanoparticles. A detailed protocol of the procedure can be found in Ref. [27]. A 25 nm thick W was sputtered onto the substrate, and then a lift-off procedure was performed to obtain the W nanodiscs. The diameter of the top W nanodisc is 240 nm. All SEM images were taken by a Zeiss 1540 XB machine.

2.2. Reflectivity measurements

Emissivity spectra of the W nanodisc emitter in the visible and near-infrared regions were measured using a PerkinElmer Lambda 1050 ultraviolet–visible–near infrared (UV–Vis–NIR) spectrometer with a 150 mm integrating sphere. The incident light (with a minimum angle of incidence of 8°) was unpolarized. Reflection measurements were performed in the optical range of 300–2300 nm with a spectral resolution of 3 nm, and a labsphere spectralon reflectance standard was used for normalization. The polarization sensitivity of the W nanodisc structures was investigated with Glan–Taylor air-spaced polarizers. A variable angle reflectance center mount holder attached to the integrating sphere was used to measure the angular sensitivity of the W nanodiscs. A Fourier transform infrared spectrometer (FTIR-Vertex 70, Bruker) was used to perform mid-infrared spectral measurements in the range of 2–10 μm.

2.3. Emissivity measurements

According to Kirchhoff's law of thermal radiation, the emissivity of a hot radiating body equals its absorptivity; thus, the TPV-relevant spectral emissivity is deduced by measuring the absorptivity. The absorptivity/emissivity is obtained by $\alpha/\varepsilon = 1 - \rho - \tau$, where ρ and τ are reflectivity and transmissivity, respectively. Since $\tau = 0$ for an optically thick (150 nm) W film, the emissivity is directly deduced by the reflectivity: $\varepsilon = 1 - \rho$.

2.4. Finite-difference time-domain simulations

To simulate the emissivity spectra and near-field distributions of the W nanodisc emitter, a commercial software (FDTD Solution, Lumerical Inc., Vancouver, Canada) was used. The optical constants of W was taken from Palik data [32]. A unit-cell of 4×4 μm^2 containing 18 W nanodiscs was constructed by investigating the SEM images. An x-polarized plane wave was irradiated on the structure.

A 5 nm mesh grid size was used all over the simulation region, and the incident plane wave source was polarized along the x-direction. For short-range ordered W nanodiscs, periodic boundary conditions were used along the x- and y-directions while perfectly matched layer (PML) boundary condition was applied along the z-direction.

2.5. Thermal stability

High-temperature annealing experiments were performed in a tube furnace. Initially, a diaphragm vacuum pump was used to obtain mTorr level vacuum before introducing the forming gas (5% H_2 and 95% Ar). The forming gas flows continuously in the tube furnace during the annealing process. Forming gas reduces oxides on the metal surfaces and convert them into water. The substrates were heated at various temperatures for 24 h with a maximum of 1200 °C. The temperature was ramped at a rate of 10 °C min^{-1}.

3. Results and discussion

A schematic presentation of the W nanodisc emitter, consisting of a metal-insulator-metal configuration, is shown in Fig. 1a, where $d_{Al_2O_3}$ denotes the thickness of the Al_2O_3 film. A normal-incidence scanning-electron micrograph (SEM) of the emitter with $d_{Al_2O_3} = 150$ nm is shown in Fig. 1b and S1. Fig. 2a shows the measured emissivity spectra of the W nanodisc emitter for various $d_{Al_2O_3}$. When $d_{Al_2O_3}$ is 50 nm, spectral resonance is observed around 500 nm wavelength. By increasing $d_{Al_2O_3}$, the spectral resonance is red-shifted. Once $d_{Al_2O_3}$ reaches 150 nm, the observed spectral resonance with a maximum emissivity above 90% is

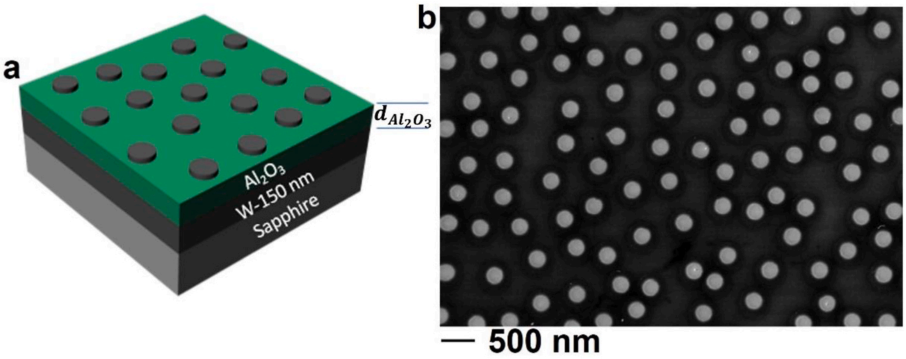

Fig. 1. (a) Schematic presentation of W nanodisc emitter and the corresponding normal-incidence SEM image is shown in (b).

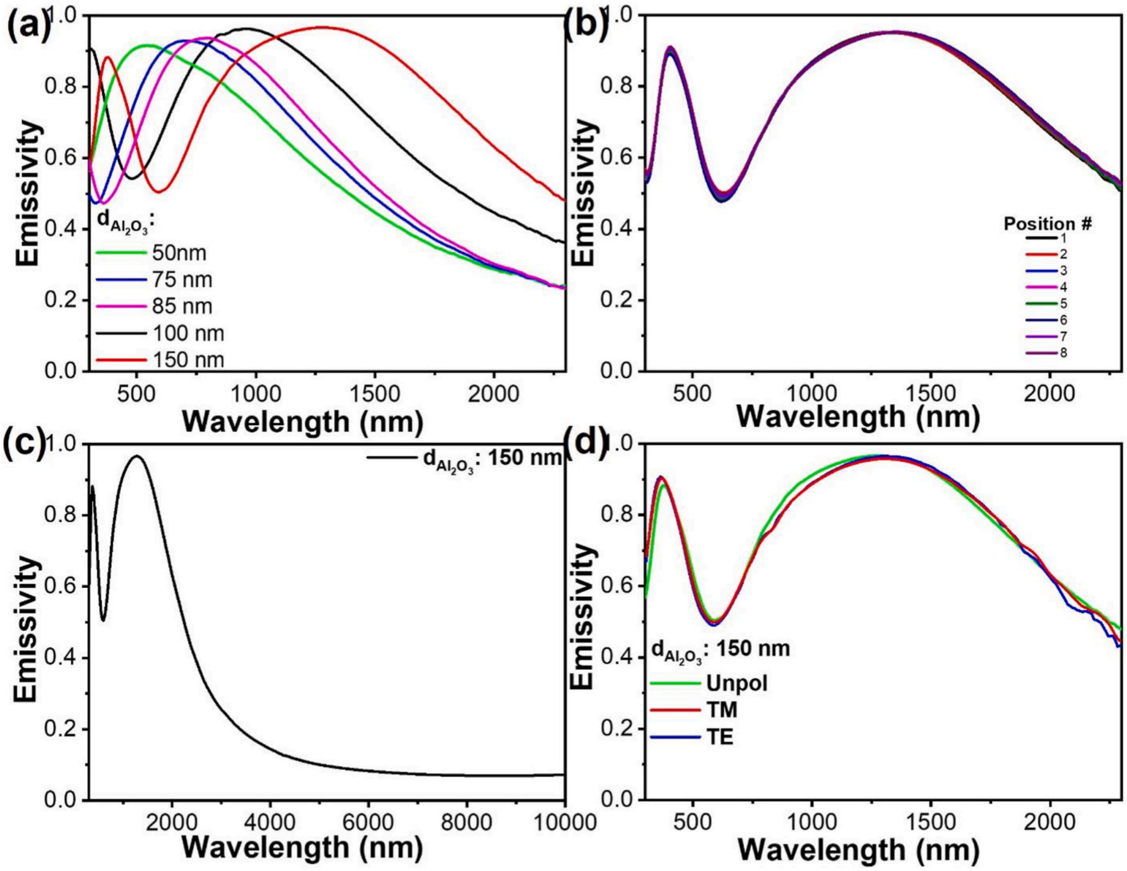

Fig. 2. (a) Measured ε spectra of the W nanodisc emitter. (b) Measured ε spectra were taken at eight different nonoverlapping spatial positions of the substrate, where a beam diameter of 1 mm is used in the UV–vis–NIR spectrometer. (c) Measured ε spectrum of the emitter for $d_{Al_2O_3} = 150$ nm in the UV–Vis-MIR spectral region. (d) Measured ε spectra of the emitter (for $d_{Al_2O_3} = 150$ nm) recorded with unpolarized as well as TM and TE polarized light. All the emissivity measurements were taken at room temperature.

seen around 1340 nm wavelength.

Fig. 3a shows the calculated emissivity spectra using FDTD simulations, which are identical to the measured spectra in terms of spectral resonance position and emissivities (Figs. 2a and 3a and S2). To reveal the underlying mechanism of strong emissivity at spectral resonances, the electric and magnetic field ($|E|$ and $|\mathrm{H}|$) distributions at two peaks (i.e., 390 and 1340 nm) are shown for the emitter with a spacer thickness $d_{Al_2O_3}$ of 150 nm in Fig. 3b. The short wavelength resonance at $\lambda_1 \approx 390$ nm is a Fabry−Pérot (FP) resonance supported by a symmetric FP cavity, where the electric field is distributed between W nanodiscs and the resonance wavelength is mainly determined by the thickness of the middle spacer (Fig. 3a). The long-wavelength resonance at $\lambda_2 \approx 1340$ nm is the localized surface plasmon resonance, it is determined by both the spacer thickness and the nanodisc diameter. Specifically, the electric dipole resonance is excited on the nanodiscs along the *x*-axis under the *x*-polarized excitation (Fig. 3b). Meanwhile, the magnetic field is mainly concentrated within the gap between the W nanodiscs and the continuous W film.

Fig. 2b shows the emissivity spectra taken at eight different spatial locations of the W nanodisc emitter. Although the deposition gives a stochastic formation of W nanodisc patterns, the emissivity variation is very minimal owing to the low-Q resonators formed by the W nanodiscs [12,20,33]. W contains a positive real part of the complex dielectric permittivity and an imaginary part on par with the magnitude of the real

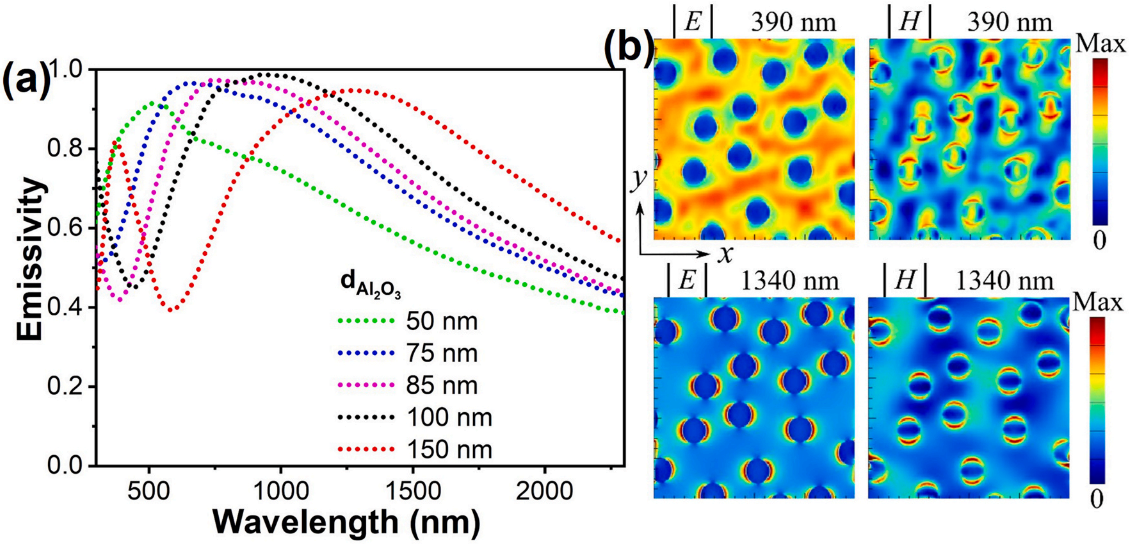

Fig. 3. (a) Calculated emissivity spectra of the emitter, with a variation in $d_{Al_2O_3}$ between 50 nm and 150 nm using the room temperature optical properties of the W. (b) Electric and magnetic field distributions at the *x-y* plane for the modes at 390 nm and 1340 nm wavelengths.

part in the visible region. However, W exhibits a negative real part of the complex dielectric permittivity in the near-far infrared regions. Therefore, W nanodiscs exhibit resonance modes with a wide bandwidth in the visible-to-near-infrared regions due to the low-Q resonators formed by the lossy W. Despite of the short-range-ordered W nanodiscs, uniform emissivity spectra are observed when measured at various locations of the sample.

The measured emissivity spectrum from UV–Vis to mid-infrared regions for the $d_{Al_2O_3} = 150$ nm emitter is shown in Fig. 2c, where the emissivities are below 10% in the near-mid infrared spectral region. Fig. 2d shows the emissivity spectra of the emitter ($d_{Al_2O_3} = 150$ nm) with unpolarized, transverse magnetic (TM), and transverse electric (TE) polarized light. The observed spectra for TM and TE polarizations show a negligible variation compared to unpolarized light, owing to the low Q-factor resonator formed by the lossy W. Further, the polarization invariance and angle independence (varies between 0° and 80° for TM and TE polarizations) emissivity of the emitter is shown in Fig. (4a and 4b). In the case of TM polarization, the emissivities of the structure is well above 90% around the spectral position of 1340 nm for the oblique incidence angles up to 65° and then decreases to 80% for the oblique incidence angle of 80°. Whereas for TE polarization, high emissivities are observed up to 65°, and then a gradual decrement is noticed at higher incidence angles. Fig. S3 shows the calculated emissivities for oblique angle incidences at TM and TE polarizations. A good agreement is observed between the measured and calculated emissivities.

The thermal stability of the W nanodisc emitters is investigated by annealing them in an Ar atmosphere under ambient pressure. Fig. 5 shows emissivity spectra of the W nanodisc emitter for as-fabricated, and after annealing at high temperatures between 1000 °C and 1200 °C for 24 h duration, and the corresponding SEM images are shown in Fig. 6. After annealing the emitter at 1000 °C, no significant change in the emissivities is observed, compared to the as-fabricated structure, except for a slight change in the spectral features of the annealed structure due to thermally induced structural changes, such as grain growth. Such a change in the spectral position is typically observed when the thin films are deposited at room temperature and exposed to high temperatures for the first time [20]. Fig. S4 shows the SEM image of the emitter after annealing at 1000 °C, and it clearly shows no sign of structural degradation. The SEM image in Fig. 6b shows no structural degradation in the W nanodisc geometry nor Al_2O_3 film. However, after annealing at 1100 °C, the emissivity spectrum is identical to the structure annealed at 1000 °C, though an increment in the emissivity is noticed around 1800 nm spectral position. The SEM images (Fig. 6c, e and S5, S6) clearly show smearing edges in the W nanodisc and local bulging in the Al_2O_3

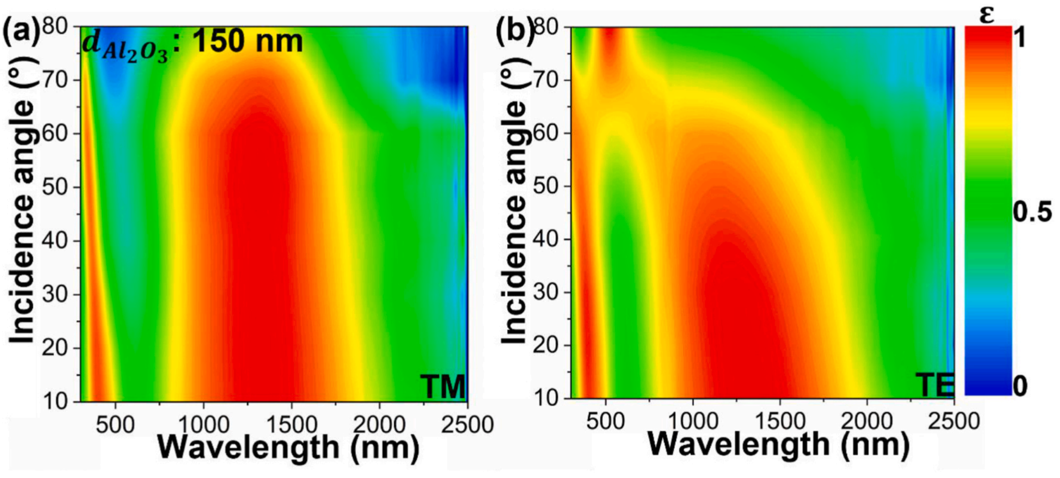

Fig. 4. (a and b) Experimental ε of the emitter for $d_{Al_2O_3} = 150$ nm as a function of spectral wavelength and incidence angle for TM and TE polarizations.

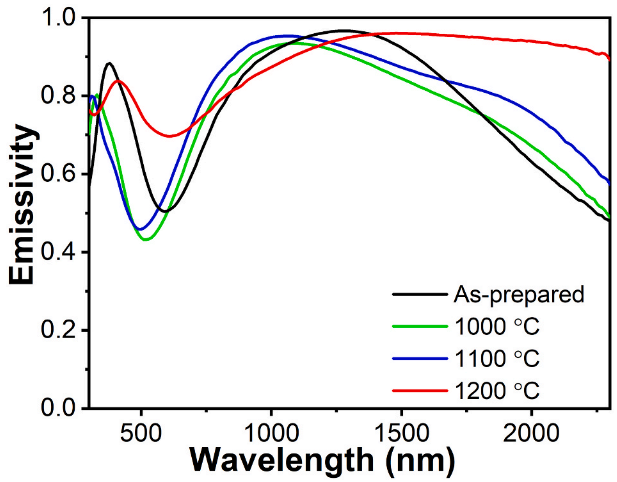

Fig. 5. Emissivity spectra of the W nanodisc emitter (for $d_{Al_2O_3} = 150$ nm) are measured at room temperature, for as-fabricated, and after annealing at high temperatures up to 1200 °C for 24 h.

film. Nevertheless, a complete degradation in spectral selectivity is only observed after annealing at 1200 °C, and the corresponding SEM images in Fig. 6(d, f, and g) and S7 show structural changes in the Al_2O_3 film, formation of hills and valleys due to thermal stress.

The spectral efficiency η is calculated, Fig. 7, as a function of the temperature T and PV cell bandgap energy E_g. η provides the efficiency of the emitter particularly, however, the efficiency of TPV energy harvesting system much differs from spectral efficiency, and it includes other factors such as cavity efficiency, quantum efficiency, fill factor, etc [34].

η is defined as the ratio of the convertible thermal radiation energy in the PV cell to the total radiated thermal energy by the emitter, as follows [5,35,36]

$$\eta = \int_{E_g}^{\infty} \frac{E_g}{E} \varepsilon(E) I_{BB}(E,T)dE \Bigg/ \int_{0}^{\infty} \varepsilon(E) I_{BB}(E,T)dE \qquad \text{(Eq. 1)}$$

where ε, E, and I_{BB} correspond to the spectral emissivity, incident thermal photon energy and blackbody spectral power density at the emitter temperature, respectively. For a photon with $E > E_g$, the excess energy is lost through thermalization. This energy can be expressed as $E_{th} = E - E_g$. For each photon, the fraction of energy lost by thermalization is then $\frac{E_{th}}{E} = 1 - \frac{E_g}{E}$. Therefore, the remaining fraction of energy converted into electricity is $1 - \frac{E_{th}}{E} = \frac{E_g}{E}$.

For comparison, the spectral efficiency of a blackbody radiator is also shown in Fig. 7a. At 800 °C, the blackbody efficiency is around 11% for a PV cell bandgap of 0.55 eV, and when the blackbody temperature is raised to 1100 °C the efficiency is increased to 22%. Whereas the η of a W nanodisc emitter shows 33% at 800 °C, for a PV cell bandgap of 0.55 eV, and 45% at 1100 °C, which is 2 × higher than for a blackbody radiator operating at 1100 °C. Notably, the pronounced decrease of the sub-bandgap photon emissions at near- and mid-infrared wavelengths (Fig. 2c); therefore, W nanodisc selective emitters perform better than a non-selective blackbody radiator.

The calculated spectral efficiencies of the different selective emitters [4,5,7,9,10,12,20,23,37–39] are compared with W nanodisc emitter (Fig. 8, where the emissivity data is extracted to calculate η) for an operating temperature and PV cell bandgap of 1100 °C and 0.55 eV, respectively. η of the W nanodisc emitter is on par with the state-of-the-art selective emitters, where most of the reported emitters were fabricated using lithography patterning and advanced etching/deposition techniques. The inherent complexities and resource requirements of the emitter fabrication restrict its usability, thereby confining its applications primarily to lab research. W nanodisc emitter excels in terms of the simple and large-area nanofabrication route, making it highly effective in large-scale deployment of TPV energy harvesting systems.

4. Conclusions

In summary, W nanodisc-based spectrally-selective emitters were demonstrated for thermophotovoltaic energy harvesting by scalable and cost-effective nanofabrication methods. The emitter structure exhibits wide-angle invariance and polarization insensitivity. Spectral tunability is obtained by tailoring the Al_2O_3 film thickness. The emitter exhibits low emissivities (below 10%) in the mid-infrared region. FDTD simulations corroborate that the LSPR of the W nanodisc, together with the spacer thickness, is accountable for the observed spectral selectivity. To investigate the usability of the W nanodisc emitters in thermophotovoltaic energy harvesting, the thermal stability of the emitter is analyzed by heat treating the emitter at high temperatures. Annealing the emitter at 1000 °C under ambient pressure and Ar atmosphere leaves no change in spectral selectivity and structural stability. A slight variation in the emissivity is observed at 1100 °C, and complete degradation of spectral

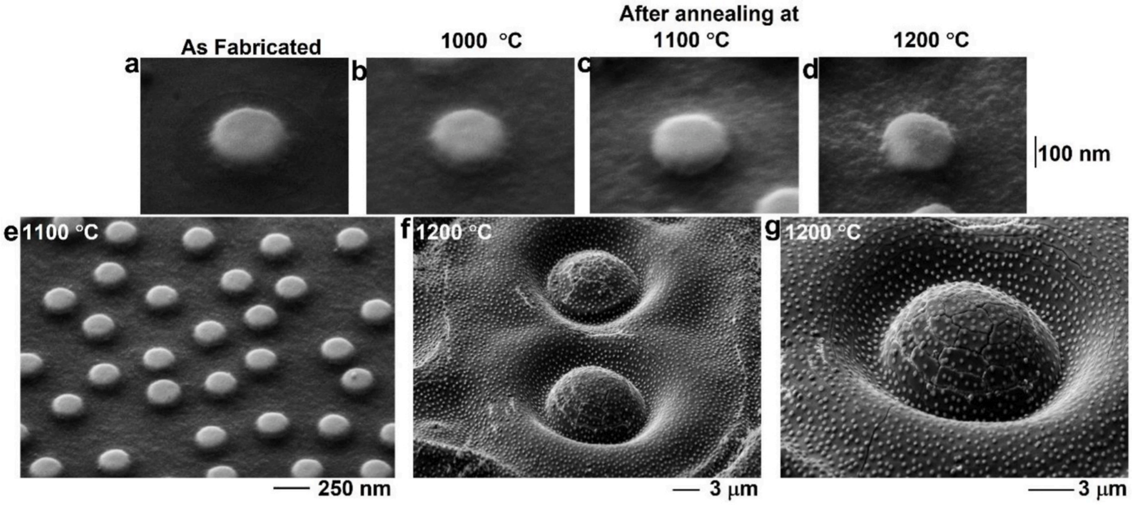

Fig. 6. SEM images at 54° tilted view of the nanodisc structure for as-fabricated, and after annealing at 1000 °C, 1100 °C and 1200 °C for 24 h. All SEM images (a–d) share the same scale bar. (e–g) Magnified views of the nanodiscs after annealing at 1100 °C and 1200 °C.

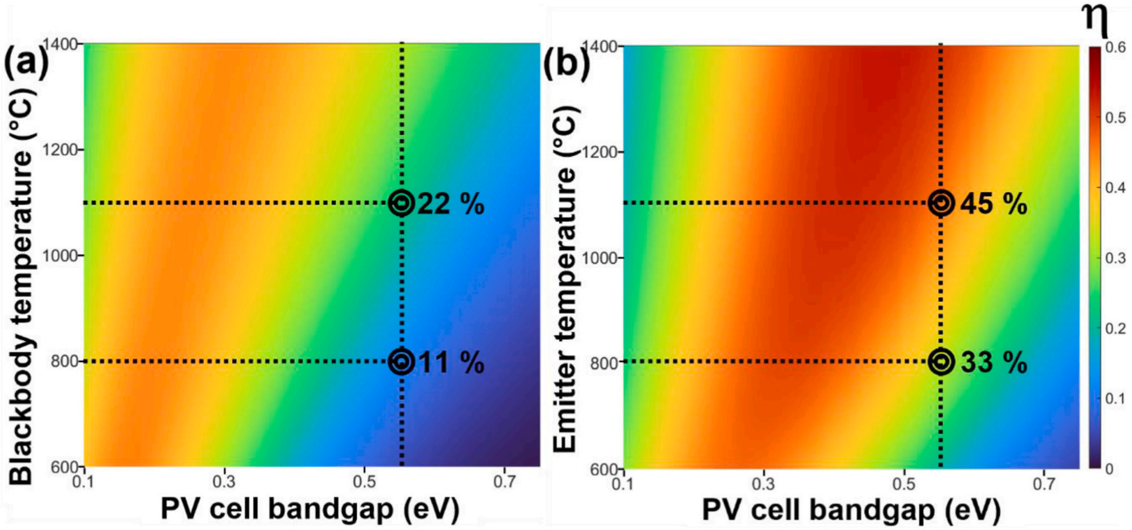

Fig. 7. (a and b) Contour maps show the calculated spectral efficiency η of blackbody and W nanodisc emitter, respectively, for temperature versus PV cell bandgap energy. The dotted vertical line represents the bandgap of the InGaAsSb PV cell at 0.55 eV.

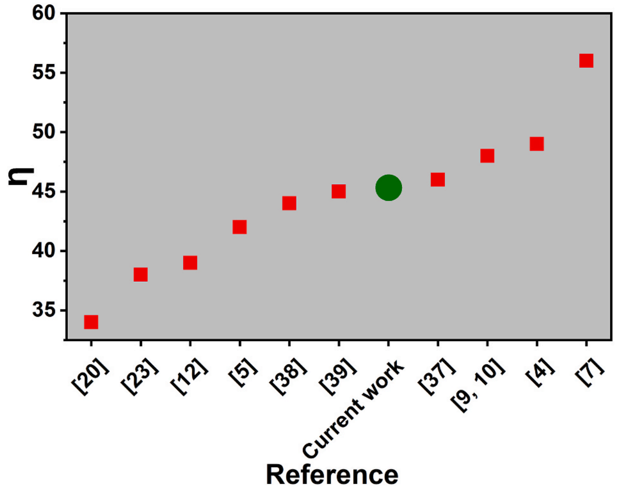

Fig. 8. Calculated η of the selective emitters [4,5,7,9,10,12,20,23,37–39] at an operating temperature of 1100 °C and a PV cell bandgap of 0.55 eV.

selectivity is observed at 1200 °C owing to structural changes in the Al_2O_3 film. Since the emitter structure contains all refractory materials, changing the deposited spacer layer from Al_2O_3 to HfO_2, this structure can be operated at temperatures higher than 1400 °C, which will be the scope of a future publication. Therefore, the utilization of easily implementable fabrication methods to produce selective emitters represents a significant stride in achieving the scalability of TPV energy harvesting technology for widespread implementation on a large scale.

CRediT authorship contribution statement

Anisha Chirumamilla: Writing – review & editing, Writing – original draft, Visualization, Resources, Methodology, Investigation, Formal analysis. **Fei Ding:** Methodology, Formal analysis. **Yuanqing Yang:** Methodology, Formal analysis. **Murugan Senthil Mani Rajan:** Methodology, Formal analysis. **Sergey I. Bozhevolnyi:** Writing – review & editing, Supervision. **Duncan S. Sutherland:** Writing – review & editing, Supervision. **Kjeld Pedersen:** Writing – review & editing, Supervision. **Manohar Chirumamilla:** Writing – review & editing, Supervision, Project administration, Conceptualization.

Declaration of competing interest

The authors declare that they have no known competing financial interests or personal relationships that could have appeared to influence the work reported in this paper.

Data availability

No data was used for the research described in the article.

Acknowledgements

M. Chirumamilla acknowledges the financial support from the Deutsche Forschungsgemeinschaft (DFG, German Research Foundation) via SFB 986 ‘Tailor-Made Multi-Scale Materials Systems: M3’, Project-ID 192346071, project C1. M. Chirumamilla and K. Pedersen acknowledge the financial support from the Novo Nordisk, grant number NNF20OC0064735. F. Ding acknowledges the support from Villum Fonden (grant no. 37372) and Independent Research Fund Denmark (project no. 1134-00010B). We thank Prof. Etienne Blandre (Junia-ISEN, France) for the fruitful discussion on TPV.

Appendix A. Supplementary data

Supplementary data to this article can be found online at https://doi.org/10.1016/j.solmat.2023.112449.

References

[1] A. LaPotin, K.L. Schulte, M.A. Steiner, K. Buznitsky, C.C. Kelsall, D.J. Friedman, E. J. Tervo, R.M. France, M.R. Young, A. Rohskopf, S. Verma, E.N. Wang, A. Henry, Thermophotovoltaic efficiency of 40, Nature 604 (2022) 287–291.

[2] E.J. Tervo, R.M. France, D.J. Friedman, M.K. Arulanandam, R.R. King, T. C. Narayan, C. Luciano, D.P. Nizamian, B.A. Johnson, A.R. Young, L.Y. Kuritzky, E. E. Perl, M. Limpinsel, B.M. Kayes, A.J. Ponec, D.M. Bierman, J.A. Briggs, M. A. Steiner, Efficient and scalable GaInAs thermophotovoltaic devices, Joule 6 (2022) 2566–2584.

[3] B. Lee, R. Lentz, T. Burger, B. Roy-Layinde, J. Lim, R.M. Zhu, D. Fan, A. Lenert, S. R. Forrest, Air-bridge Si thermophotovoltaic cell with high photon utilization, ACS Energy Lett. 7 (2022) 2388–2392.

[4] M. Shimizu, T. Furuhashi, Z. Liu, H. Yugami, Highly confined spectrally selective absorber-emitter for effective solar thermophotovoltaics, Sol. Energy Mater. Sol. Cells 245 (2022), 111878.

[5] K. Cui, P. Lemaire, H. Zhao, T. Savas, G. Parsons, A.J. Hart, Tungsten–carbon nanotube composite photonic crystals as thermally stable spectral-selective absorbers and emitters for thermophotovoltaics, Adv. Energy Mater. 8 (2018), 1801471.

[6] L. Wei, G. Urcan, K. Nathaniel, G.V. N, B. Alexandra, G. Jianguo, V.M. S, A.V. K, Refractory plasmonics with titanium nitride: broadband metamaterial absorber, Adv. Mater. 26 (2014) 7959–7965.

[7] V. Rinnerbauer, A. Lenert, D.M. Bierman, Y.X. Yeng, W.R. Chan, R.D. Geil, J. J. Senkevich, J.D. Joannopoulos, E.N. Wang, M. Soljačić, I. Celanovic, Metallic photonic crystal absorber-emitter for efficient spectral control in high-temperature solar thermophotovoltaics, Adv. Energy Mater. 4 (2014), 1400334.

[8] P.N. Dyachenko, S. Molesky, A.Y. Petrov, M. Störmer, T. Krekeler, S. Lang, M. Ritter, Z. Jacob, M. Eich, Controlling thermal emission with refractory epsilon-near-zero metamaterials via topological transitions, Nat. Commun. 7 (2016), 11809.

[9] M. Chirumamilla, G.V. Krishnamurthy, K. Knopp, T. Krekeler, M. Graf, D. Jalas, M. Ritter, M. Störmer, A.Y. Petrov, M. Eich, Metamaterial emitter for thermophotovoltaics stable up to 1400 °C, Sci. Rep. 9 (2019) 7241.

[10] M. Chirumamilla, G.V. Krishnamurthy, S.S. Rout, M. Ritter, M. Störmer, A. Y. Petrov, M. Eich, Thermal stability of tungsten based metamaterial emitter under medium vacuum and inert gas conditions, Sci. Rep. 10 (2020) 3605.

[11] T. Krekeler, S.S. Rout, G.V. Krishnamurthy, M. Störmer, M. Arya, A. Ganguly, D. S. Sutherland, S.I. Bozhevolnyi, M. Ritter, K. Pedersen, A.Y. Petrov, M. Eich, M. Chirumamilla, Unprecedented thermal stability of plasmonic titanium nitride films up to 1400 °C, Adv. Opt. Mater. 9 (2021), 2100323.

[12] D.N. Woolf, E.A. Kadlec, D. Bethke, A.D. Grine, J.J. Nogan, J.G. Cederberg, D. Bruce Burckel, T.S. Luk, E.A. Shaner, J.M. Hensley, High-efficiency thermophotovoltaic energy conversion enabled by a metamaterial selective emitter, Optica 5 (2018) 213–218.

[13] D.M. Bierman, A. Lenert, W.R. Chan, B. Bhatia, I. Celanović, M. Soljačić, E. N. Wang, Enhanced photovoltaic energy conversion using thermally based spectral shaping, Nat. Energy 1 (2016), 16068.

[14] Z. Utlu, Thermophotovoltaic applications in waste heat recovery systems: example of GaSb cell, Int. J. Low Carbon Technol. 15 (2020) 277–286.

[15] D. Feng, S.K. Yee, Z.M. Zhang, Improved performance of a near-field thermophotovoltaic device by a back gapped reflector, Sol. Energy Mater. Sol. Cells 237 (2022), 111562.

[16] Z. Omair, G. Scranton, L.M. Pazos-Outón, T.P. Xiao, M.A. Steiner, V. Ganapati, P. F. Peterson, J. Holzrichter, H. Atwater, E. Yablonovitch, Ultraefficient thermophotovoltaic power conversion by band-edge spectral filtering, Proc. Natl. Acad. Sci. USA 116 (2019) 15356–15361.

[17] R. Sakakibara, V. Stelmakh, W.R. Chan, M. Ghebrebrhan, J.D. Joannopoulos, M. Soljacic, I. Čelanović, Practical emitters for thermophotovoltaics: a review, J. Photon. Energy 9 (2019), 032713.

[18] C. Ferrari, F. Melino, M. Pinelli, P.R. Spina, M. Venturini, Overview and status of thermophotovoltaic systems, Energy Proc. 45 (2014) 160–169.

[19] D. Chubb, Fundamentals of Thermophotovoltaic Energy Conversion, Elsevier Science, Amsterdam, 2007.

[20] C.-C. Chang, W.J.M. Kort-Kamp, J. Nogan, T.S. Luk, A.K. Azad, A.J. Taylor, D.A. R. Dalvit, M. Sykora, H.-T. Chen, High-temperature refractory metasurfaces for solar thermophotovoltaic energy harvesting, Nano Lett. 18 (2018) 7665–7673.

[21] J.B. Chou, Y.X. Yeng, Y.E. Lee, A. Lenert, V. Rinnerbauer, I. Celanovic, M. Soljačić, N.X. Fang, E.N. Wang, S.-G. Kim, Enabling ideal selective solar absorption with 2D metallic dielectric photonic crystals, Adv. Mater. 26 (2014) 8041–8045.

[22] J.G. Fleming, S.Y. Lin, I. El-Kady, R. Biswas, K.M. Ho, All-metallic three-dimensional photonic crystals with a large infrared bandgap, Nature 417 (2002) 52.

[23] K.A. Arpin, M.D. Losego, A.N. Cloud, H. Ning, J. Mallek, N.P. Sergeant, L. Zhu, Z. Yu, B. Kalanyan, G.N. Parsons, G.S. Girolami, J.R. Abelson, S. Fan, P.V. Braun, Three-dimensional self-assembled photonic crystals with high temperature stability for thermal emission modification, Nat. Commun. 4 (2013) 2630.

[24] R. Sakakibara, V. Stelmakh, W.R. Chan, R.D. Geil, S. Krämer, T. Savas, M. Ghebrebrhan, J.D. Joannopoulos, M. Soljačić, I. Čelanović, A high-performance, metallodielectric 2D photonic crystal for thermophotovoltaics, Sol. Energy Mater. Sol. Cells 238 (2022), 111536.

[25] Y. Zhu, G. Hou, Q. Wang, T. Zhu, T. Sun, J. Xu, K. Chen, Silicon-based spectrally selective emitters with good high-temperature stability on stepped metasurfaces, Nanoscale 14 (2022) 10816–10822.

[26] X. Liu, T. Tyler, T. Starr, A.F. Starr, N.M. Jokerst, W.J. Padilla, Taming the blackbody with infrared metamaterials as selective thermal emitters, Phys. Rev. Lett. 107 (2011), 045901.

[27] H. Fredriksson, Y. Alaverdyan, A. Dmitriev, C. Langhammer, D.S. Sutherland, M. Zäch, B. Kasemo, Hole–mask colloidal lithography, Adv. Mater. 19 (2007) 4297–4302.

[28] A. Chirumamilla, Y. Yang, M.H. Salazar, F. Ding, D. Wang, P.K. Kristensen, P. Fojan, S.I. Bozhevolnyi, D.S. Sutherland, K. Pedersen, M. Chirumamilla, Spectrally selective emitters based on 3D Mo nanopillars for thermophotovoltaic energy harvesting, Mater. Today Phys. 21 (2021), 100503.

[29] M. Chirumamilla, A. Chirumamilla, Y. Yang, A.S. Roberts, P.K. Kristensen, K. Chaudhuri, A. Boltasseva, D.S. Sutherland, S.I. Bozhevolnyi, K. Pedersen, Large-area ultrabroadband absorber for solar thermophotovoltaics based on 3D titanium nitride nanopillars, Adv. Opt. Mater. 5 (2017), 1700552.

[30] M. Chirumamilla, A.S. Roberts, F. Ding, D. Wang, P.K. Kristensen, S.I. Bozhevolnyi, K. Pedersen, Multilayer tungsten-alumina-based broadband light absorbers for high-temperature applications, Opt. Mater. Express 6 (2016) 2704–2714.

[31] M. Arya, A. Ganguly, G.V. Krishnamurthy, S.S. Rout, L. Gurevich, T. Krekeler, M. Ritter, K. Pedersen, M. Störmer, A. Yu Petrov, M. Eich, M. Chirumamilla, Which factor determines the optical losses in refractory tungsten thin films at high temperatures? Appl. Surf. Sci. 588 (2022), 152927.

[32] E.D. Palik, Handbook of Optical Constants of Solids III, Academic Press, Burlington, 1997.

[33] A.S. Roberts, T. Søndergaard, M. Chirumamilla, A. Pors, J. Beermann, K. Pedersen, S.I. Bozhevolnyi, Light extinction and scattering from individual and arrayed high-aspect-ratio trenches in metals, Phys. Rev. B 93 (2016), 075413.

[34] Z. Wang, D. Kortge, Z. He, J. Song, J. Zhu, C. Lee, H. Wang, P. Bermel, Selective emitter materials and designs for high-temperature thermophotovoltaic applications, Sol. Energy Mater. Sol. Cells 238 (2022), 111554.

[35] N. Jeon, J.J. Hernandez, D. Rosenmann, S.K. Gray, A.B.F. Martinson, J.J. Foley IV, Pareto optimal spectrally selective emitters for thermophotovoltaics via weak absorber critical coupling, Adv. Energy Mater. 8 (2018), 1801035.

[36] J.J. Foley, C. Ungaro, K. Sun, M.C. Gupta, S.K. Gray, Design of emitter structures based on resonant perfect absorption for thermophotovoltaic applications, Opt. Express 23 (2015) A1373–A1387.

[37] E. Blandre, M. Shimizu, A. Kohiyama, H. Yugami, P.-O. Chapuis, R. Vaillon, Spectrally shaping high-temperature radiators for thermophotovoltaics using Mo-HfO2 trilayer-on-substrate structures, Opt. Express 26 (2018) 4346–4357.

[38] N. Jeon, D.J. Mandia, S.K. Gray, J.J.I.V. Foley, A.B.F. Martinson, High-temperature selective emitter design and materials: titanium aluminum nitride alloys for thermophotovoltaics, ACS Appl. Mater. Interfaces 11 (2019) 41347–41355.

[39] J.H. Kim, S.M. Jung, M.W. Shin, Thermal degradation of refractory layered metamaterial for thermophotovoltaic emitter under high vacuum condition, Opt. Express 27 (2019) 3039–3054.